INSTITUTE OF PHYSICS PUBLISHING JOURNAL OF PHYSICS D: APPLIED PHYSICS

J. Phys. D: Appl. Phys. **34** (2001) 3164–3176 PII: S0022-3727(01)26866-1

Spatio-temporally resolved spectroscopic diagnostics of the barrier discharge in air at atmospheric pressure

K V Kozlov[1], H-E Wagner[2], R Brandenburg[2] and P Michel[2]

[1] Moscow State University, Department of Chemistry, 119899 Moscow, Russia
[2] Institute of Physics, Ernst-Moritz-Arndt University of Greifswald, 17489 Greifswald, Domstrasse 10a, Germany

E-mail: kozlov@kge.msu.ru and wagner@physik.uni-greifswald.de

Received 13 July 2001
Published 23 October 2001
Online at stacks.iop.org/JPhysD/34/3164

Abstract

The technique of spatially resolved cross-correlation spectroscopy (CCS) is used to carry out diagnostic measurements of the barrier discharge (BD) in air at atmospheric pressure. Quantitative estimates for electric field strength $E(x, t)$ and for relative electron density $n_e(x, t)/n_e^{max}$ are derived from the experimentally determined spatio-temporal distributions of the luminosity for the spectral bands of the 0–0 transitions of the second positive system of N_2 ($\lambda = 337.1$ nm) and the first negative system of N_2^+ ($\lambda = 391.5$ nm). These results are used to test the validity of some physical models of electrical breakdown in a BD. The influence of the spatio-temporal structure of the discharge on the chemical kinetics of ozone synthesis is studied by means of a semi-empirical method based on the results of spatially resolved CCS measurements.

1. Introduction

Experimental and theoretical study of barrier discharges (BDs, sometimes also referred to as dielectric barrier discharges or silent discharges) has a long history [1, 2] in connection with their wide industrial application in ozone generation technologies [3]. However, despite of considerable progress in understanding the structure and properties of these discharges, which principally occurred during the last few decades, the knowledge of this subject nowadays appears to be insufficient to provide an adequate quantitative theoretical description for BD behaviour [4].

A BD in oxygen as well as in air consists of a number of microdischarges (MDs, sometimes also referred to as partial discharges [5] or discharge filaments [1]) of nanosecond duration, randomly but uniformly distributed over the dielectric surface [1, 2]. Under the typical conditions for operation of a BD (discharge gap width of $d = 1$–2 mm; dielectric, glass of $\Delta = 1$–2 mm thickness and dielectric constant $\varepsilon = 5$–7; gas pressure $p = 1$–3 bar), these MDs can be treated as tiny plasma-chemical reactors that act independently from one another [1, 2, 6, 7]. That is why the study of the dynamics of a single MD is one of the most important research topics in the field of BD physics and chemistry. It is hard to carry out any experiment with a single MD, since high temporal resolution (in a sub-nanosecond range) and spatial resolution (down to 10^{-1}–10^{-2} mm) is required. Moreover, in the case of the commonly used parallel-plane electrode arrangement, it is usually impossible to predict the location at which a MD will emerge.

Thus, it is understandable that much effort has been devoted to computer simulation of MD development [1, 2, 4, 7–15]. As regards experimental findings, the following important milestones should be mentioned: 1972, identification of separate MDs [5]; 1980, streak photography of a single MD [16, 17]; 1983, accurate measurement of MD current pulses [18]; 1995, determination of spectrally resolved spatio-temporal distributions of MD luminosity by means of the cross-correlation spectroscopy (CCS) technique [19, 20]. It should be mentioned that the authors [19] also used their experimental data for a qualitative characterization of the spatio-temporal structure of an electric field within a MD channel.

The idea of quantitatively estimating the electric field strength in gas discharges in air at atmospheric pressure from experimentally determined distributions of the emission intensities of both the second positive (0–0) band of N_2

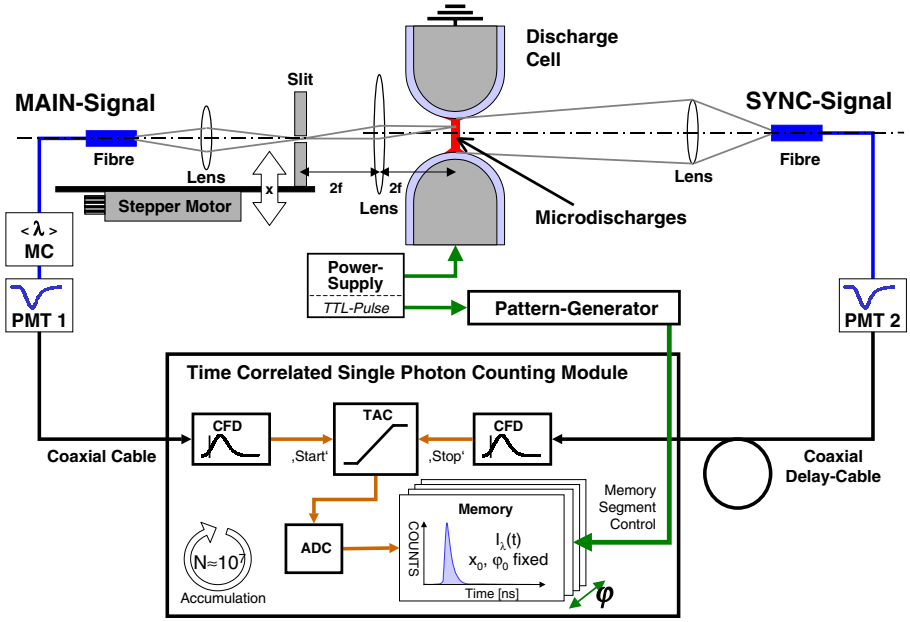

Figure 1. A general diagram of the apparatus and measurement procedure: MC, monochromator; PMT, photomultiplier; TTL, transistor–transistor logic; CFD, constant fraction discriminator; TAC, time-to-amplitude converter; ADC, analogue-to-digital converter; φ, phase of the feeding sinusoidal voltage (see figure 2).

and the first negative (0–0) band of N_2^+ has recently been proposed [21–23]. However, as yet this potentially powerful method of plasma diagnostics has not been used in practice, since no arrays of experimental data with the required sensitivity and spatio-temporal resolution were available.

Our preliminary experiments on the BD investigation by CCS have shown that this technique is able to comply with the requirements mentioned earlier [24]. In the present paper, we report the results of an accomplished procedure of a BD plasma diagnostics by means of spatially resolved CCS, including the quantitative estimation of the electric field, relative electron density and ozone yield within a MD channel. All these measurements and calculations have been performed for a BD with a symmetrical electrode arrangement (the so-called two-sided BD, i.e. 'glass–glass'), discharge gap width of 1.2 mm, in flowing synthetic air (80%N_2 + 20%O_2) at atmospheric pressure, i.e. under the typical conditions of ozone generation technologies.

The plan of this paper is as follows. The apparatus and experimental technique are described in detail in section 2. Particular attention is paid to the procedure of CCS measurements. In section 3, the experimental results are presented and discussed with respect to their contribution to understanding the physical mechanism of MD development. The procedure for the quantitative numerical analysis of experimental data together with the corresponding estimation of MD parameters are presented in section 4. These data are compared to the results of computer modelling, available from the literature, and the observed discrepancies are discussed.

2. Equipment and experimental technique

The main idea of the method of CCS is to replace a direct measurement of the single pulse of luminosity from a repetitive light pulse emitter by a statistically averaged determination of the correlation function between two optical signals, both originating from the same source. The first of these signals (the so-called 'synchronizing signal') is used to define a relative time scale, the second one (the 'main signal') has to be detected with a probability at least one order of magnitude lower than that of the synchronizing signal. The measured quantity is actually a time delay between these two signals, and the recorded quantity is a probability density function for the evolution of the light pulse intensity. If the repetitive light pulses reproduce each other sufficiently exactly, and if the synchronizing signal detection is adjusted in such a way as to occur always at the same moment that a single light pulse evolves, then the recorded probability density function is proportional to the light intensity $I(t)$ of the source under consideration. A detailed description of the theoretical foundations of the CCS technique is given in [25].

A general scheme of the experimental set-up and measurement procedure is presented in figure 1. In our experiments, the BD itself (more precisely, the successive MDs arising between the electrode tips) was used as the emitter of repetitive light pulses. The spatial resolution and scanning over the MD axis were provided by the optical system shown in the left-hand upper part of the figure. The monochromatic light of the main signal was detected by a highly sensitive photomultiplier from Hamamatsu (type H5773-04), which operated in a single-photon-counting mode. In order to increase the sensitivity of this detector by reducing the noise-to-signal ratio, it was cooled down to +12 °C. The second detector for the synchronizing signal (Hamamatsu, type H5773-06, shown in the figure on the right-hand side) was adjusted so as to reach the maximal possible temporal resolution of the steep front of a light pulse, since the derivative of this signal is actually used to define the zero-point of the relative time scale.

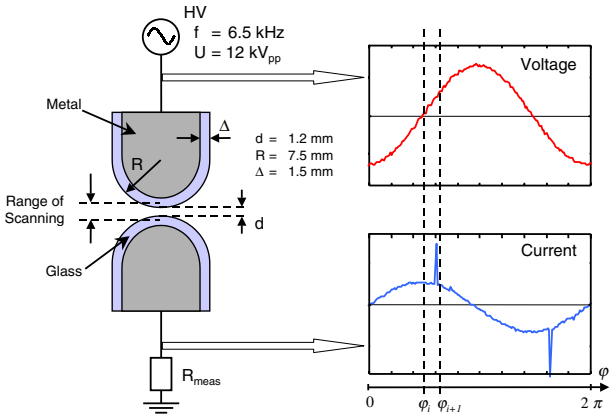

Figure 2. Electrode arrangement with the indicated range of axial scanning and a typical example of the oscillograms of voltage and current for the 'one-to-one MD' operation mode.

The measurements of the correlation functions and accumulation of the results were carried out by the time-correlated single-photon-counting module SPC–530 from Becker and Hickl GmbH. An outline of the measurement procedure is presented at the bottom of the figure 1. Two constant fraction discriminators are used to select the electric pulses which belong to a pre-defined range of amplitudes. A selected pulse from the main signal initiates a linear rise in the voltage of the time-to-amplitude converter, and the next pulse (which is selected from the synchronizing signal) stops this rise. The measured quantity is the final voltage amplitude. This value is converted to the number of the corresponding time channel of the device (actually, to a memory address), and a unit is added to this channel. The entire scale of the memory segment consists of 1024 channels. If no synchronizing signal arises and the voltage of the time-to-amplitude converter reaches its upper limit, then no count occurs. The correspondence between the time value and the number of the time channel is determined by the duration of the voltage rise, which varies from 50 ns to 2 μs. A shift in the zero-point to the left over the time axis is possible due to the insertion of a coaxial delay cable between the detector for the synchronizing signal and module SPC-530.

An additional, coarse time scale was provided by the pattern generator which was synchronized with the phase of the feeding voltage φ by a standard scheme of transistor–transistor logic (see figures 1 and 2). The voltage duration time (154 μs) was divided into 16 equal time intervals, and a separate memory segment was used to record the CCS measurements for each of these intervals. Thus, for any fixed position of the detector, the time-correlated measurement results were accumulated simultaneously in 16 memory segments. Typically, up to 10^7 counts were accumulated in the memory segment with a maximal count rate for a measurement 5 min in duration.

In order to localize the BD in a definite position, we used a special electrode arrangement of the type 'glass–glass' (figure 2), similar to those described earlier by the authors [16, 17, 19, 20]. One more advantage of such a geometry for the discharge cell is the possibility of observing not only the volume part of the BD but also the surface discharges, provided that the range of axial scanning exceeds the gap width.

The BD was driven by a sinusoidal alternating voltage (frequency, 6.5 kHz; peak-to-peak amplitude, 12 kV). The voltage amplitude was adjusted so as to maintain the discharge in the 'one-to-one MD' mode (i.e. a mode when only one MD occurs per voltage half-period, as shown in figure 2).

All experiments were performed in an open gas flow system, in synthetic air ($80\%N_2+20\%O_2$) at ambient pressure. The gas flow rate was maintained at 54 l h^{-1}. Assuming energetic yield of ozone to be lower than 100 g kWh^{-1} [2, 3], and taking into account the measured value of the discharge power ($P = 0.095$ W), the upper possible limit of ozone concentration under the experimental conditions under consideration can be evaluated. This value appears to be about 0.01%. According to the results [26], the ozone has a noticeable influence on the spatio-temporal structure of MDs for ozone concentrations greater than 0.1%.

The main characteristics of our CCS measurements are summarized in table 1. It should be noted that the values of the fine resolution over time given there refer to the apparatus parameters. Actually, these values depend on the quality of synchronization. Under the conditions of our experiments, the real time resolution for the 50 ns scale has been found to be no worse than 0.15 ns (see section 4 for more details).

3. Experimental results and their interpretation

All CCS measurements were recorded simultaneously into 16 memory segments corresponding to the coarse time scale, as described earlier. The distribution of the count rates over this scale reveals the distribution of the MDs over the voltage phase (see figure 2). In our experiments, the MDs were found to appear mostly within two to four time intervals for every half-period (each divided into eight intervals). Apart from the signal amplitudes, no noticeable differences between the spatio-temporal structures of the luminosity of the MDs, corresponding to the different time intervals of the same half-period, have been observed. The structures referring to the opposite polarities of the electrodes were symmetrical with respect to the spatial axis, as was expected taking into account the symmetry of the electrode arrangement. In the following, the measurement results only refer to one time interval of the coarse scale (to that one with the maximal count rate).

3.1. Spectrum and spatio-temporal structure of the MD luminosity

An emission spectrum of the BD was recorded under the previously described experimental conditions within the wavelength range 200–800 nm. It has been found to consist of several spectral bands of the second positive system of N_2, and the only one band of the first negative system of N_2^+ (0–0 transition, $\lambda = 391.5$ nm). In figure 3, part of this spectrum is presented.

Spatio-temporal distributions of the MD luminosity for three selected spectral bands are shown in figure 4. Each of these plots contains two peaks situated near the electrodes and related to nearly the same time coordinate. The peaks near the cathode are preceded by the waves of light intensity, that

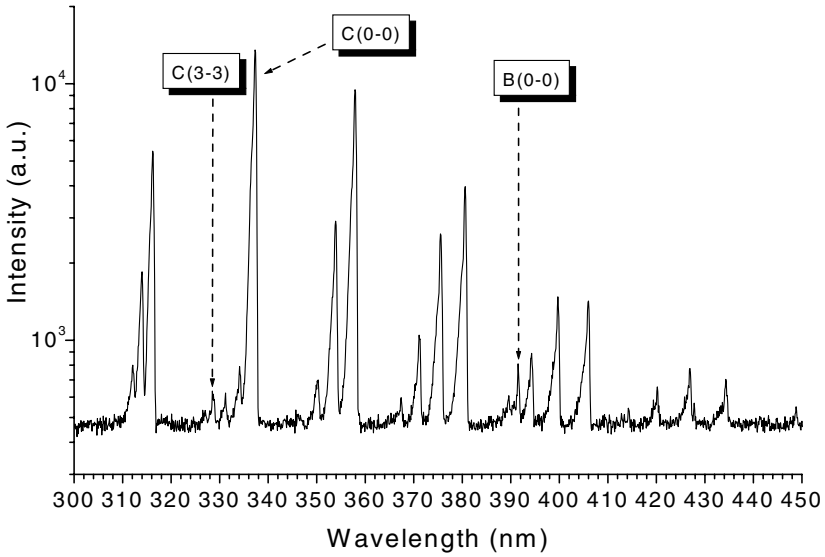

Figure 3. Spectrum of the BD in air ($p = 1$ bar, $d = 1.2$ mm). The bands used for the spatially and temporally resolved measurements are indicated.

Table 1. Basic parameters of the CCS measurements.

Quantity	Range of scanning/scale	Resolution
Time (coarse scale, PPG)	154 μs/16	$\sim$10 μs/memory segment
Time (fine scale, CCS)	50 ns–2 μs/1024	0.05 ns–2 ns/channel
Space (axial direction)	2 mm/20	0.1 mm/record
Space (radial direction)	—	0.2 mm
Wavelength	200–800 nm/6000	0.3 nm

start directly from the anode surface and propagate towards the cathode with increasing velocity and growing amplitude. The ratio of the peak intensities I (cathode)/I (anode) rises drastically in the sequence of spectral bands C (0–0), C (3–3), B (0–0).

To interpret these results, it is necessary to consider the origin of the light sources within a MD channel. For the spectral bands C (0–0), C (3–3), B (0–0), the emission of light of the corresponding wavelengths is caused by the elementary processes (1)–(6):

$$\mathrm{e} + \mathrm{N}_2(\mathrm{X}\,^1\Sigma_g^+)_{v=0} \longrightarrow \mathrm{N}_2(\mathrm{C}\,^3\Pi_u)_{v'=0} + \mathrm{e} \quad (\Delta E = 11.0\ \mathrm{eV}) \tag{1}$$

$$\mathrm{N}_2(\mathrm{C}\,^3\Pi_u)_{v'=0} \longrightarrow \mathrm{N}_2(\mathrm{B}\,^3\Pi_g)_{v''=0} + h\nu \quad (\lambda = 337.1\ \mathrm{nm},\ \tau_0^C = 40\ \mathrm{ns}) \tag{2}$$

$$\mathrm{e} + \mathrm{N}_2(\mathrm{X}\,^1\Sigma_g^+)_{v=0} \longrightarrow \mathrm{N}_2(\mathrm{C}\,^3\Pi_u)_{v'=3} + \mathrm{e} \quad (\Delta E = 11.8\ \mathrm{eV}) \tag{3}$$

$$\mathrm{N}_2(\mathrm{C}\,^3\Pi_u)_{v'=3} \longrightarrow \mathrm{N}_2(\mathrm{B}\,^3\Pi_g)_{v''=3} + h\nu \quad (\lambda = 328.5\ \mathrm{nm}) \tag{4}$$

$$\mathrm{e} + \mathrm{N}_2(\mathrm{X}\,^1\Sigma_g^+)_{v=0} \longrightarrow \mathrm{N}_2^+(\mathrm{B}\,^2\Sigma_u^+)_{v'=0} + 2\mathrm{e} \quad (\Delta E = 18.7\ \mathrm{eV}) \tag{5}$$

$$\mathrm{N}_2^+(\mathrm{B}\,^2\Sigma_u^+)_{v'=0} \longrightarrow \mathrm{N}_2^+(\mathrm{X}\,^2\Sigma_g^+)_{v''=0} + h\nu \quad (\lambda = 391.5\ \mathrm{nm},\ \tau_0^B = 60\ \mathrm{ns}). \tag{6}$$

In air at atmospheric pressure, a stepwise excitation of molecular and ionized nitrogen is hardly possible because of very effective collisional quenching of excited states by molecular oxygen [21–23, 27]. Therefore only direct electron impact is taken into account in the kinetic scheme (1)–(6). For the same reason, the characteristic lifetimes of the considered excited states in air are less than 1 ns, while their radiation lifetimes (τ_0) are within the range 40–60 ns (see section 4 for more details). Therefore, the spatio-temporal distributions of the intensity of light emission (2), (4) and (6) follow the reaction rates of (1), (3) and (5), respectively, with a time lag less than 1 ns. These reaction rates are directly proportional to electron density, while the rate constants are strongly dependent on electric field [21–23, 27]. Furthermore, under the conditions of non-equilibrium weakly ionized plasmas in air at atmospheric pressure, the mean electron energy is within the range of a few electronvolts [1, 2, 7, 12, 21, 27]. Hence, it is only a very small fraction of electrons that possess energies that exceed the threshold values of the reactions (1), (3) and (5). In such a case, a higher threshold energy gives a stronger dependence of the corresponding rate constant on the electric field [21–23].

Thus, a qualitative analysis of the results presented in figure 4 leads to the following conclusions. The wave of light intensity, which is observed most clearly for the spectral band B (0–0) with a threshold energy of approximately 19 eV, reveals an electric field wave (ionizing wave, or streamer [2, 16, 17, 19, 20]). The two peaks of the luminosity distributions differ physically, namely, there is a higher electric field and a lower electron density near the cathode than near the anode.

A similar way of reasoning can be applied to the results presented in figure 5. The electron current density within a MD channel is equal to the product of elementary charge,

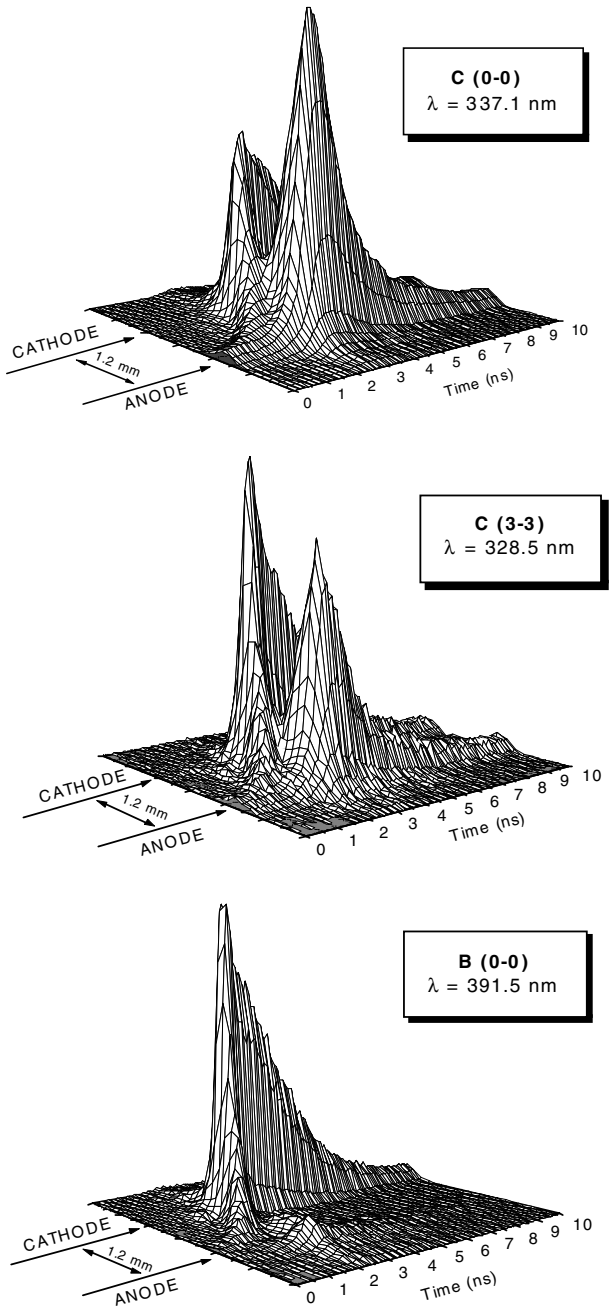

Figure 4. A general view of the luminosity distributions over time and space for three different spectral bands of nitrogen indicated on figure 3.

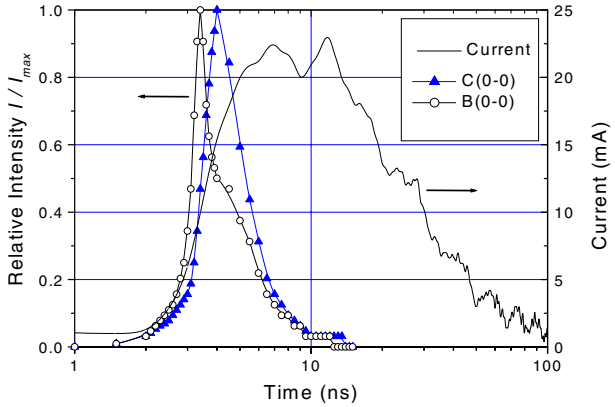

Figure 5. Current pulse of the MD and the light pulses corresponding to the spectral bands indicated in figure 3.

concentration and the drift velocity of the electrons, the latter quantity being nearly proportional to the electric field strength. Hence, a slow decrease in electric field may be expected to result in a current decay of a comparable characteristic time and, in contrast, to cause a rapid fall in the light intensity. Furthermore, it should be taken into account that a measured MD current includes the ion currents as well, and that the contributions of the ion components increase during the decay phase, as the electrons leave the MD volume.

As regards the results plotted in figure 5, the following important remarks should be made. Both light pulses are integral quantities. They have been calculated as the corresponding sums of the spatially resolved CCS data over the entire range of axial scanning. These pulses are synchronized with each other. In contrast, the current pulse has not been synchronized with the light pulses, i.e. it has an arbitrary position on the time scale of the plot. An accurate measurement of the MD current was outside the scope of this work. Thus, no special effort has been made to avoid the over-vibrations (these can be clearly seen in figure 5), as well as to determine a real value of the current rise-time, which may be expected not to exceed 1 ns [2, 28]. However, in spite of the mentioned drawbacks of the MD current measurement, our results provide sufficient accuracy at least for the evaluation of the half-width of the pulse (20–25 ns).

3.2. Mechanism of the MD origin and development

A great advantage of the CCS technique is its high sensitivity. Moreover, this method enables reliable measurement of a very weak light intensity simultaneously with a strong signal at the same time scale of the time-to-amplitude converter. Thus, it is better to represent experimental results in a logarithmic scale, in order to visualize all the details of the spatio-temporal distributions of the MD luminosity. Such representations for the spectral bands C (0–0) and B (0–0) are shown in figure 6. These are the same experimental data as in figure 4, but the time scale is extended up to 40 ns.

The process of electrical breakdown of the discharge gap (see the central parts of the plots in figure 6, which are also shown in figure 4 in more detail), is preceded by a weak but continuously growing glow on the anode which is clearly seen for the spectral band C (0–0). The maximal intensity of this glow is observed at the place corresponding to the position of the electrode tip.

During the post-breakdown phase of the MD development, the sources of light are situated mainly on both dielectric surfaces, but the spatial distributions of the intensities are different for the two spectral bands under consideration (see figure 6). The long 'tail' of luminosity on the cathode observed for the first negative system of nitrogen may be considered as an indication of the relatively high electric field remaining on the dielectric surface after the breakdown.

In order to study the pre-breakdown phase of the MD in more detail (in particular, to determine its duration), we have

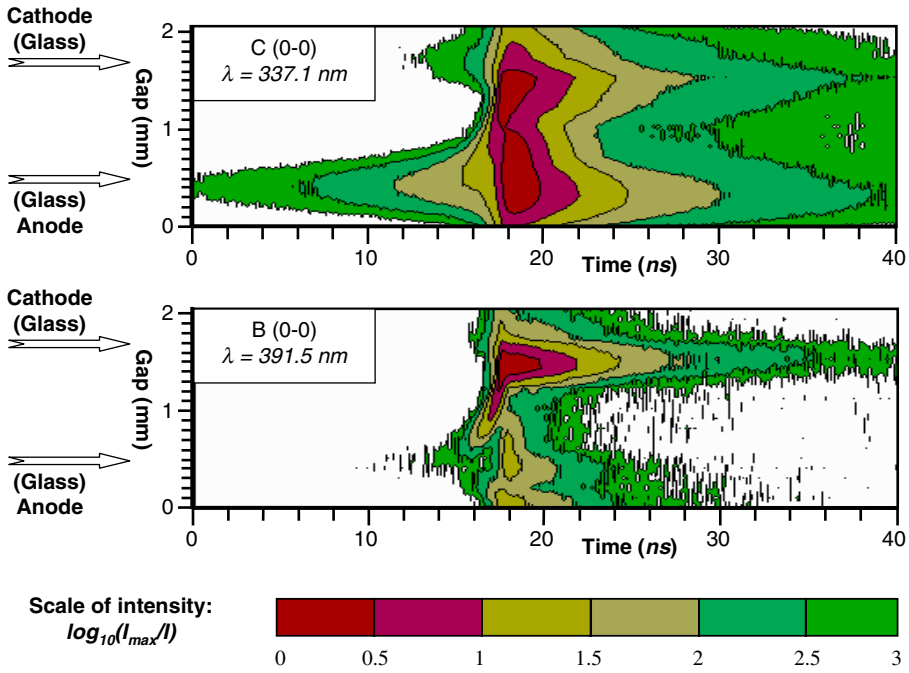

Figure 6. Spatio-temporal distributions of the luminosity for the 0–0 transitions of the second positive (upper plot) and of the first negative (lower plot) systems of nitrogen. The positions of the electrode tips (see figure 2) are indicated on the left by the arrows.

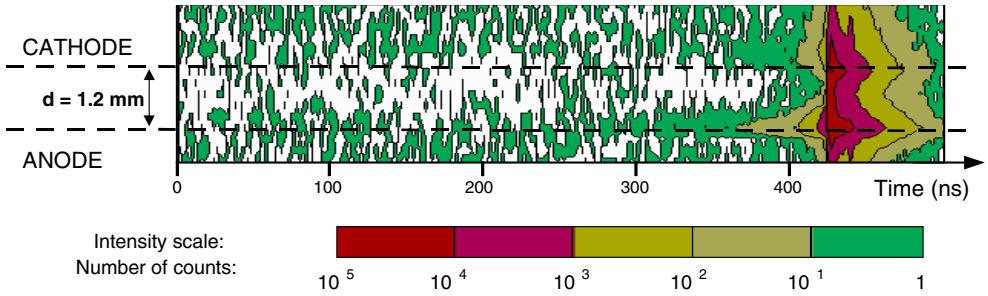

Figure 7. Pre-breakdown phase of the MD development. Spectral band C (0–0), $\lambda = 337.1$ nm. The positions of the electrode tips (see figure 2) are indicated by the broken lines.

undertaken a special experiment. The time scale of the CCS instrument has been extended to 500 ns, while the duration of each measurement at a fixed spatial point has been lengthened to 30 min. The results of these measurements are shown in figure 7.

For the period of 100–150 ns before the breakdown, a maximal light intensity is observed at the position of the anode tip. For the earlier time period, the light sources seem to be distributed almost uniformly over the entire visible surface of both electrodes, while the luminosity of the discharge gap appears to be noticeably lower. It should be noted that in the measurements under consideration, a sensitivity limit of the CCS technique has been reached. Namely, the count rates corresponding to the first 200 ns of the time scale and referring to the central part of the spatial scanning range (i.e. to the discharge gap, see figure 7), has been found to be comparable to the background level (dark count rate).

Any information concerning the pre-breakdown phase of a MD is very important for a correct understanding of its origin and development [4]. In fact, in the modern theory of BDs there are two alternative physical models of the MD in an ozonizer (i.e. in a BD in oxygen or in air). Both claim either to agree with experimental findings at least qualitatively [17, 26, 28, 29], or to provide a correct theoretical description for the process under consideration, when explicitly or implicitly used in computer simulations [7, 10–15]. The diagrams in figure 8 represent these two models.

According to model A (see figure 8), a cathode-directed ionizing wave (a cathode streamer) is initiated by the distortion of electric field by the positive space charge accumulated within the MD channel. Accumulation of positive ions in the gap takes place during the pre-breakdown phase of the MD development, when initial electron avalanches cross the gap [7, 10–12, 17]. It can even be the only avalanche containing a sufficient number of electrons to cause field distortion, as was assumed by the authors of [13–15]. Model A implies the following initial conditions. There is no surface charge on the dielectrics, hence the initial electric field is uniform. The initial electric field strength is equal to the corresponding Paschen value, therefore ionization dominates over electron attachment.

Model B assumes the existence of surface charges that are non-uniformly distributed over the dielectrics. These charges

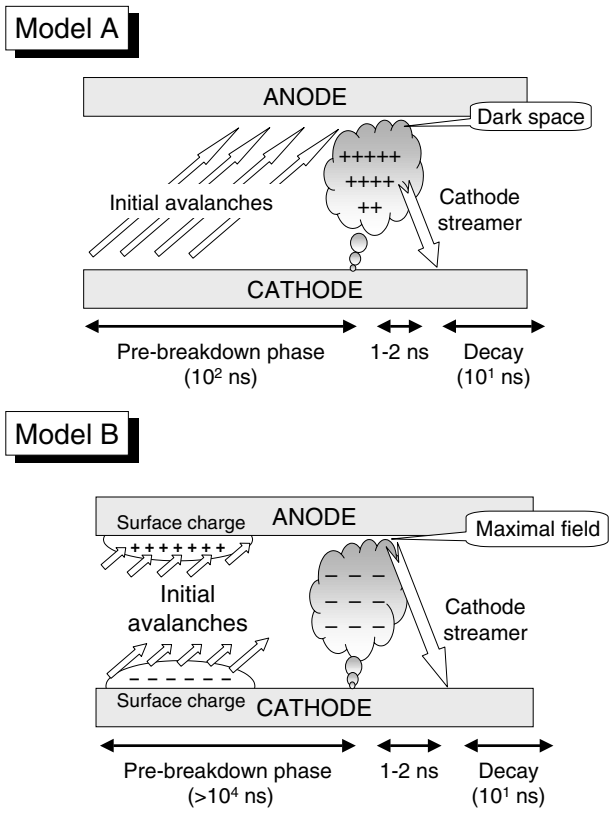

Figure 8. Two alternative physical models of the MD mechanism, that have been proposed in the literature [4, 10, 17, 28, 29].

are expected to cause local enhancement of the electric field near the electrodes, while the field strength in the middle part of the gap is supposed to remain as low, as to provide domination of electron attachment. The pre-breakdown phase of the MD can last for a period of several microseconds [19, 29]. Under such conditions, the development of the local electron avalanches result in an accumulation of the negative space charge within the MD channel [28]. This space charge causes a distortion of the electric field near the anode and the cathode-directed streamer starts.

There are at least two differences between models A and B that might be observed in the corresponding spatio-temporal distributions of the MD luminosity. First, during the pre-breakdown phase of the MD, there might be either an exponential growth of the light intensity in the direction from the cathode to the anode (model A); or a more complicated axial distribution of the luminosity with two local maximums situated on the dielectric surfaces (model B). Second, in the case of model A, a cathode-directed streamer should be expected to start at a certain distance from the anode, where a field enhancement between the positive space charge and the negatively charged cathode takes place. Moreover, at the same time, a dark space should be observed between the positive space charge and the positively charged anode, where the initial electric field is obviously lower (see figure 8). It should be noted that such behaviour by the MD luminosity is clearly seen on the 'simulated streak photos' obtained by means of computer modelling with initial conditions, corresponding to model A [7, 12–14]. In model B, a maximal field strength (hence, the starting point of the streamer) should be expected directly on the surface of the anode (see figure 8).

Thus, our results presented in figures 4, 6, 7 and considered here, provide unambiguous experimental evidence in favour of model B. Taking into account the initial conditions, assumed for model A, we may expect this model to describe some special cases of a BD operation. For example, it can account for the first electrical breakdown event in an ozonizer (i.e. at the moment when an ozonizer is just switched on), since only at this moment are there no surface charges on the dielectrics. Also, in some laboratory experiments, the BD was operated in a special single-pulse mode, when the periodical slow voltage pulses were applied to the discharge cell. In order to remove a surface charge, a rest-time interval of about 30 min between the successive single pulses was provided [17]. Obviously, for an ordinary (continuous) operation mode of a BD, model B should be used.

4. Quantitative numerical analysis of the experimental data

4.1. Kinetic scheme and basic data sets used in the analysis

In the following, only the kinetics of the two excited states of nitrogen ($N_2(C\,^3\Pi_u)_{v'=0}$) and ($N_2^+(B\,^2\Sigma_u^+)_{v'=0}$) is considered. The kinetic scheme (1), (2), (5) and (6) described in detail in section 3.1, should be completed by the addition of the processes of collisional quenching [21–23, 27]:

$$N_2(C\,^3\Pi_u)_{v'=0} + N_2/O_2 \xrightarrow{K^C_{N_2}/K^C_{O_2}} \text{products} \tag{7}$$

$$N_2^+(B\,^3\Sigma_u^+)_{v'=0} + N_2/O_2 \xrightarrow{K^B_{N_2}/K^B_{O_2}} \text{products}. \tag{8}$$

According to the complete kinetic scheme (1), (2), (5)–(8), the local concentrations of the excited species ($N_2(C\,^3\Pi_u)_{v'=0}$) and ($N_2^+(B\,^2\Sigma_u^+)_{v'=0}$) denoted here, respectively, as $n_C(r,t)$ and $n_B(r,t)$, obey the following differential equations.

$$\begin{aligned}\frac{dn_C(r,t)}{dt} &= k_C(E/n)n_{N_2}(r,t)n_e(r,t)\\ &\quad -n_C(r,t)(K^C_{N_2}n_{N_2} + K^C_{O_2}n_{O_2}) - \frac{n_C(r,t)}{\tau_0^C}\\ &= k_C(E/n)n_{N_2}(r,t)n_e(r,t) - \frac{n_C(r,t)}{\tau_{air}^C}\end{aligned} \tag{9}$$

$$\begin{aligned}\frac{dn_B(r,t)}{dt} &= k_B(E/n)n_{N_2}(r,t)n_e(r,t)\\ &\quad -n_B(r,t)(K^B_{N_2}n_{N_2} + K^B_{O_2}n_{O_2}) - \frac{n_B(r,t)}{\tau_0^B}\\ &= k_B(E/n)n_{N_2}(r,t)n_e(r,t) - \frac{n_B(r,t)}{\tau_{air}^B}\end{aligned} \tag{10}$$

Here k_C and k_B are the rate constants of the reactions (1) and (5), respectively, that are treated as sole functions of the reduced field strength E/n. $n_e(r,t)$, n_{N_2} and n_{O_2} are the electron density and concentrations of molecular nitrogen and oxygen in the ground electronic states, respectively. The characteristic lifetimes τ_{air}^C and τ_{air}^B of the excited electronic states ($N_2(C\,^3\Pi_u)_{v'=0}$) and ($N_2^+(B\,^2\Sigma_u^+)_{v'=0}$) in air are defined as shown in expressions (9) and (10).

Table 2. Overview of the $N_2(C)$ and $N_2^+(B)$ de-excitation rate coefficients, available in the literature.

Second positive system of nitrogen (0–0)				
τ_0^C (ns)	$K_{N_2}^C$ (10^{-11} cm^3 s^{-1})	$K_{O_2}^C$ (10^{-10} cm^3 s^{-1})	τ_{air}^C (ns)	Reference
37 ± 3	1.5 ± 0.2	1.35 ± 0.13	0.96 ± 0.12	[30]
30 ± 2	1.12 ± 0.06	2.58 ± 0.18	0.55 ± 0.04	[31]
45.4	1.2	—	—	[32]
40.5 ± 1.3	1.31 ± 0.01	—	—	[33]
44.5	1.1	3.12	0.52	[34]
37 ± 4	0.9 ± 0.3	2.7 ± 0.3	0.61 ± 0.08	[35]
41 ± 2	—	—	—	[36]
—	—	—	0.58	[37]
—	—	—	<0.8	[38]
—	—	—	<0.9	This work[a]
First negative system of nitrogen (0–0)				
τ_0^B (ns)	$K_{N_2}^B$ (10^{-10} cm^3 s^{-1})	$K_{O_2}^B$ (10^{-10} cm^3 s^{-1})	τ_{air}^B (ns)	Reference
66	$2.2 - 8.2$	—	$<0.057 - 0.21$	[39]
64 ± 6	8.2 ± 1.6	—	0.059 ± 0.012	[40]
65.8	4.53	7.36	0.073	[34]
—	7.5	—	<0.062	[41]
58 ± 8	2.1 ± 0.2	5.1 ± 0.5	0.138 ± 0.013	[35]
61	—	—	—	[42]
60 ± 1	—	—	—	[43]
—	—	—	0.083	[39]
—	—	—	<0.15	This work[a]

[a] We included here own experimental estimates of effective lifetimes of $N_2(C)$ and $N_2^+(B)$ in air at atmospheric pressure. These values has been determined directly from the results of spatially resolved CCS measurements as well as the maximum slopes of decaying curves $\ln(I_{B,C}(t))$.

Experimentally detected intensities of light for the spectral bands C (0–0) and B (0–0) are directly proportional to the rates of the reactions (2) and (6), respectively.

$$I_C(r,t) = T_C \frac{n_C(r,t)}{\tau_0^C} \qquad I_B(r,t) = T_B \frac{n_B(r,t)}{\tau_0^B}. \quad (11)$$

The transmission coefficients T_C and T_B for the corresponding spectral bands are determined by the characteristics of the optical systems and by the sensitivity of the detector (figure 1). They do not depend on the spatio-temporal coordinates (r, t).

A basic formula used in the numerical analysis of our experimental data can be easily derived from equations (9)–(11):

$$\frac{k_B(E/n)}{k_C(E/n)} = \frac{\tau_0^B T_C}{\tau_0^C T_B} \frac{(\mathrm{d}I_B(r,t)/\mathrm{d}t) + (I_B(r,t)/\tau_{air}^B)}{(\mathrm{d}I_C(r,t)/\mathrm{d}t) + (I_C(r,t)/\tau_{air}^C)}. \quad (12)$$

In the right-hand part of this equation there are the quantities that can be determined from the spatially resolved CCS measurements and some rate coefficients available in the literature. On the left-hand side there is the ratio of two rate constants which can be treated as a single function of the reduced field strength. Since the dependence $k_B/k_C(E/n)$ is strong and monotonic, it can be used with equation (12) to estimate quantitatively the spatio-temporal structure of the electric field $E/n(r, t)$, provided that the resolution of the experimental technique is sufficient to avoid any considerable averaging over temporal or spatial coordinates [21–23].

Within the frame of a steady-state approximation (i.e. when the derivatives of the intensities over time in (12) may be neglected), the following simplified expression for the intensity ratio I_B/I_C may be obtained.

$$\frac{I_B(E/n)}{I_C(E/n)} = \frac{k_B(E/n)}{k_C(E/n)} \frac{\tau_0^C T_B \tau_{air}^B}{\tau_0^B T_C \tau_{air}^C}. \quad (13)$$

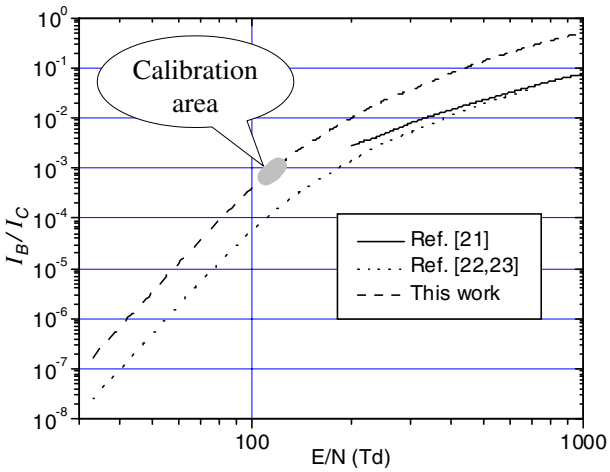

Figure 9. Dependence of the intensity ratio I_B/I_C upon the reduced field strength. The curve used in this work has been obtained by multiplying the data [22, 23] by the empirically determined factor, so as to fit the calibration results.

The authors of [21–23] proposed applying approximation (13) to estimate the electric field strength in streamer discharges in air. Using the results of the numerical solutions of the Boltzmann equation for a wide range of reduced field strength, they also calculated the dependence of the determined by (13) intensity ratio I_B/I_C upon the parameter E/n under quasi-stationary conditions (figure 9).

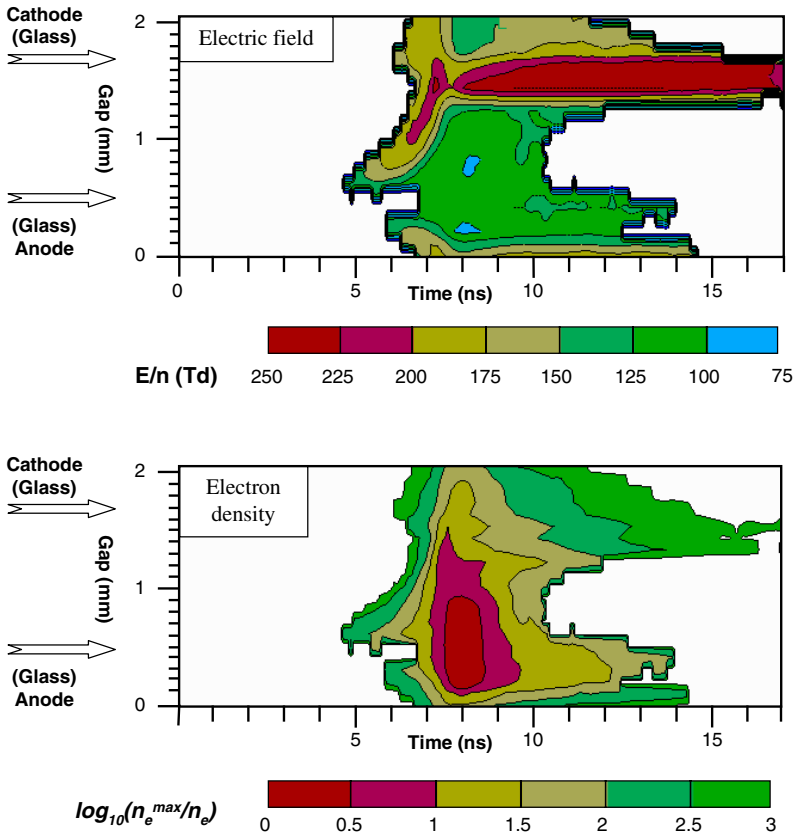

Figure 10. Calculated distributions of electric field and electron density. The outer boundary of the two-dimensional arrays of experimental data used in these calculations has been determined by the condition $(I_B, I_C) > 5$ counts/channel. The positions of the tips of the electrodes (see figure 2) are indicated by the arrows on the left.

There is a noticeable difference between the results of [21] and [22, 23], which becomes greater with a decrease in electric field strength. The values of the de-excitation rate coefficients used in equations (12) and (13) are known with an accuracy which seems to be hardly better than 10% (see table 2). Furthermore, we could not avoid some uncertainty in determining the transmission coefficients ratio T_B/T_C for our apparatus. Taking all this into account, an attempt of independent calibration for the basic function $I_B/I_C(E/n)$ has been undertaken. This calibration procedure has been accomplished as follows.

Using equation (12) we calculated the two-dimensional array of the values $k_B/k_C(x,t)$ from the experimental data. Then an area (x,t), where this ratio may be considered to be roughly constant with an accuracy of 20% was located. This area has been found to be about 2 ns long and 0.5 mm wide, corresponding to the time-space coordinate range 20–22 ns and 0.6–1.1 mm on the scales given in figure 6. Assuming a uniform and steady-state electric field within this area and using the simple approximation $I_C(x,t) = \text{constant} \times n_e(x,t)$, the mean value of the ionization coefficient α for the area under consideration was calculated. Then the electric field strength has been determined from the reference data on $\alpha(E/n)$ in [44]. Taking into account the accuracy of the previously described procedure, the corresponding 'calibration area' is indicated on the plot in figure 9.

To calculate E/n from the measured quantities I_B/I_C, the data [22, 23] were chosen (because they are available for a wider range of reduced field strength). The ratio of transmission coefficients T_B/T_C was treated as a free parameter which has been determined so as to fit with the calibration results (see figure 9).

Based on the calculated spatio-temporal distribution of the electric field, the corresponding two-dimensional array of the values of relative electron density $n_e(x,t)/n_e^{max}$ could be easily determined by means of equations (9)–(11) in a similar way, provided that not only the ratio k_B/k_C but both rate constants are well known within the same range of E/n. In these calculations, the data sets reported in [22, 23] were used.

4.2. Electrical characteristics of the microdischarge

Since the procedure of numerical differentiation of experimentally determined functions $I_{B,C}(x,t)$ over time is very sensitive to the statistical noise, a careful preliminary smoothing was carried out. Furthermore, in order to avoid any artifacts, the area of the calculations was restricted to $(I_B, I_C) > 5$ counts/channel, which was found to provide sufficient reliability and accuracy of the results. That is why the spatio-temporal distributions of electric field strength and electron density are presented in figure 10 in a smaller area than the corresponding experimental data in figure 6.

These results confirm the main conclusions derived from the qualitative analysis of the luminosity distributions in sections 3.1 and 3.2. A cathode-directed wave of electric field is clearly seen in figure 10. A high electric field strength is

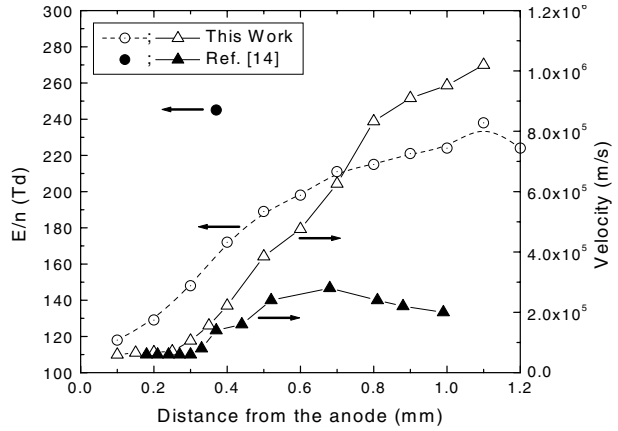

Figure 11. Comparison of the main characteristics of the cathode-directed streamer obtained in this work (open symbols) with the corresponding results of computer modelling [14] (full symbols).

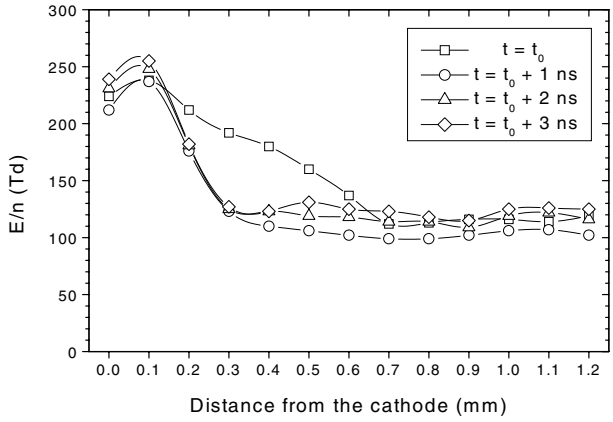

Figure 12. Evolution of the electric field strength at the beginning of the decay phase of the MD. The time $t = t_0$ refers to the moment when the streamer reaches the cathode surface.

observed mostly near the cathode, and a high electron density, in contrast, near the anode.

It is from interest to compare quantitatively some basic characteristics of the MDs corresponding to the different modes of BD operation (models A and B, see figure 8). For this purpose, two main parameters of the cathode-directed streamers have been chosen, namely the velocity and the electric field strength. Our results, as demonstrated in section 3.2, correspond to model B. As a typical example of computer simulation accomplished within the frame of model A, the two-dimensional modelling of a MD development in air at atmospheric pressure for the discharge gap of 1 mm width [14] has been chosen. The streamer velocities were determined from their tracks, that are clearly seen on the plots of the MD luminosity distribution for spectral band B (0–0) in the case of our results (figures 4 and 6), and on the simulated streak photo of the MD which is presented in [14].

Figure 11 demonstrates considerable differences between the streamers, that are supposed to develop under different initial conditions. The streamer corresponding to model B possesses a higher velocity and a lower amplitude of the local electric field. It should be noted that, qualitatively, such dependence of the streamer characteristics upon initial conditions of the MD development had been predicted recently in [28, 29] as follows.

When a cathode-directed streamer propagates through a media enriched by negative ions, a lower field is necessary to produce seed electrons before the streamer, because of effective detachment processes, and the velocity of the streamer is expected to be higher.

The results of the quantitative numerical analysis of the presented experimental data correspond not only to the streamer phase of the MD development, but also to the beginning of the decay phase (see figure 10). This part of the spatio-temporal distribution of electric field strength is shown in figure 12 in more detail.

For a period of at least 2 ns, the electric field may be treated as nearly steady-state and almost uniform within the spatial range 0.4–1.1 mm. The latter is just the space–time area which was used for the independent calibration, as described in section 4.1. It is hardly possible to present a reasonable interpretation of the local maximum of the electric field near the cathode, since at such a short distance from the electrode tip, the results of the CCS measurements are averaged over the radial axis and probably, they include light emission from the surface discharges (see figure 2).

4.3. Chemical activity of the MD plasma

In order to understand, in which way does the physics of electrical breakdown determine the efficiency of an ozonizer, it seems reasonable to begin with the analysis of the chemical mechanism of ozone synthesis in a BD plasma. The basic mechanism was established a relatively long time ago and, at present, the kinetic schemes for ozone generation in oxygen and air may be regarded as sufficiently reliable ones [1, 2]. Under the typical for an ozonizer conditions, there are only two dominant reaction channels as follows.

Ozone formation: $$O + O_2 \xrightarrow{k_{14}} O_3 + M \quad (M = O_2, N_2) \tag{14}$$

Ozone decomposition: $$O + O_3 \xrightarrow{k_{15}(T)} O_2 + O_2. \tag{15}$$

Thus, atomic oxygen can be treated as a sole precursor of ozone, and the conversion degree for the gross reaction $O + O_2 \longrightarrow O_3$ is determined by the ratio of the rate constants k_{14}/k_{15} as well as by the concentration of O_3. Due to the comparatively strong temperature dependence of the rate constant k_{15}, this conversion degree may be considerably decreased by a local temporary gas heating within the MD channel, hence it depends upon the power density profile. Obviously, a spatial distribution of the power density is determined by the spatio-temporal structure of a MD, consequently by its mechanism. This can be the first possible way to affect the chemical yield of ozone synthesis by means of influencing the characteristics of the electrical breakdown in an ozonizer.

The second way is related to the reactions leading to the formation of atomic oxygen.

$$e + O_2 \xrightarrow{k_{16}(E/n)} O + O + e \tag{16}$$

$$e + N_2 \xrightarrow{k_{17}(E/n)} N_2^* + e \qquad N_2^* + O_2 \longrightarrow N_2 + O + O. \tag{17}$$

Here the asterisk denotes the triplet excited states of molecular nitrogen ($A\,^3\Sigma_u^+$, $B'\,^3\Sigma_u^-$, $C\,^3\Pi_u$, $B\,^3\Pi_g$ and $W\,^3\Delta_u$), hence the elementary reactions (1), (3) and (7) are implicitly included in (17). According to the results [7, 12], more than 50% of the total yield of atomic oxygen in a MD channel in air at atmospheric pressure is provided by reactions (17).

Within the frame of the simplified kinetic scheme (16) and (17), the maximal possible energetic yield of atomic oxygen can be calculated as a ratio of O-atoms production rate to electric power released by drifting electrons:

$$Y_{O,max}(E/n) = \frac{k_{16}(E/n)n_{O_2} + k_{17}(E/n)n_{N_2}}{eEw_e(E/n)} \qquad (18)$$

where e is the elementary charge, and $w_e(E/n)$ is the drift velocity of electrons.

In fact, equation (18) describes the branching of electron energy losses [2, 7, 12]. In order to complete the consideration of energy losses within the MD channel, ion drift should be taken into account as well. Obviously, the contribution of ion losses also depends on the electrical breakdown mechanism and it has to be included in the general formula for energetic yield of ozone produced in a single MD:

$$Y_{Ozone}(E/n) = C\frac{\{P_e(r,t)\}}{\{P_e(r,t) + P_i(r,t)\}}\frac{\{Y_{O,max}(E/n)P_e(r,t)\}}{\{P_e(r,t)\}} \qquad (19)$$

where C is the conversion degree for the gross reaction $O + O_2 \longrightarrow O_3$ ($0 < C < 1$); the local power densities for electrons and ions are defined as

$$P_e(r,t) = en_e(r,t)E(r,t)w_e(r,t)$$

and

$$P_i(r,t) = en_i(r,t)E(r,t)w_i(r,t)$$

respectively; the parentheses { } denote integration over the entire MD volume and over the time of its existence. The right-hand part of expression (19) consists of three terms (conversion degree of O to O_3, fraction of electron energy losses and energetic yield of atomic oxygen related to electron losses), corresponding to these three different ways of the BD physics influence on the chemical efficiency of an ozonizer.

Thus, even within the frame of a simplified kinetic model (14)–(19), a detailed computer simulation of the MD development is necessary to describe quantitatively the process of ozone generation. In order to propose a qualitative description of the influence of the MD spatio-temporal structure on the kinetics of ozone synthesis, we used the following semi-empirical method. From the arrays of electric field strength $E(x,t)$ and relative electron density $n_e(x,t)/n_e^{max}$ we calculated the spatially resolved kinetics of the formation of atomic oxygen and triplet nitrogen N_2^* by the reactions (16) and (17) in a nanosecond time scale. The rate constants $k_{16}(E/n)$ and $k_{17}(E/n)$ were taken from [12]. Since we used the relative values of electron density, the results of our kinetic calculations also contain an unknown constant. However, this constant does not depend on the space–time coordinates. Therefore, thus calculated spatio-temporal distributions of the relative concentrations of considered species, that are shown in figure 13, may be expected to represent the real kinetics within the MD channel.

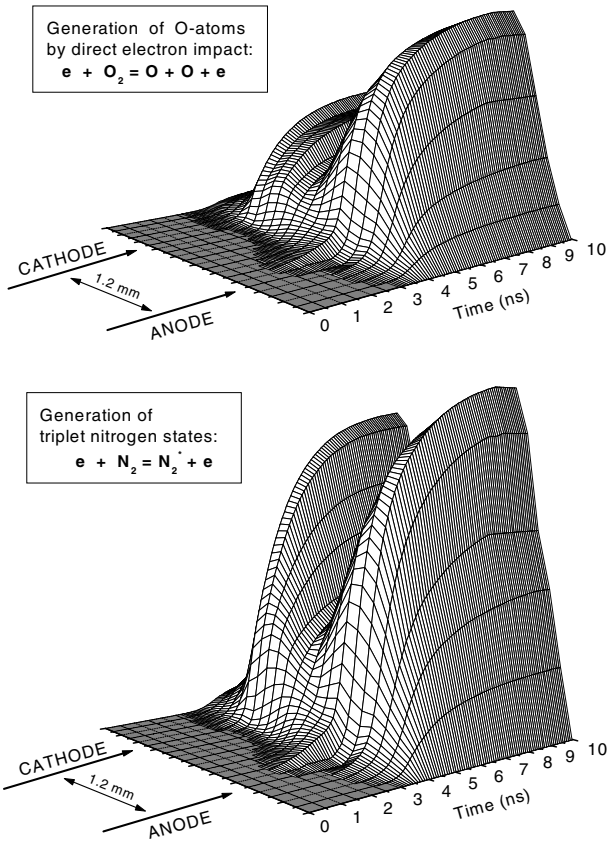

Figure 13. Calculated contributions of the two main reaction channels to the kinetics of the O-atoms generation within the MD channel.

These results show that there are two regions of high chemical activity within the MD channel. They are situated near the electrodes, corresponding to the spatio-temporal structure of the MD luminosity (compare with figure 4). Furthermore, different physical properties of these regions result in a noticeable difference in chemical kinetics. For example, as follows from figure 13, the properties of the plasma in the region near the anode, where the electric field is lower but electron density is higher than near the cathode (see figure 10), favour dissociation of molecular oxygen by direct electron impact. In the case of the excitation of triplet nitrogen states, the contributions of both regions to this process appear to be comparable.

Assuming the complete conversion of atomic oxygen to ozone ($C = 1$), the axial distribution of O_3 concentration was calculated from the data shown in figure 13. In figure 14 these results are compared with experimental data obtained in the pulse mode of BD operation [17]. Although these profiles seems to be alike, there are noticeable differences in their shapes. For example, the distribution corresponding to an ordinary mode of BD operation (our results) seems to be more uniform, and the local minimum is more near to the middle of the gap. Thus, initial conditions of a MD development exert a noticeable influence on the kinetics of ozone synthesis, too.

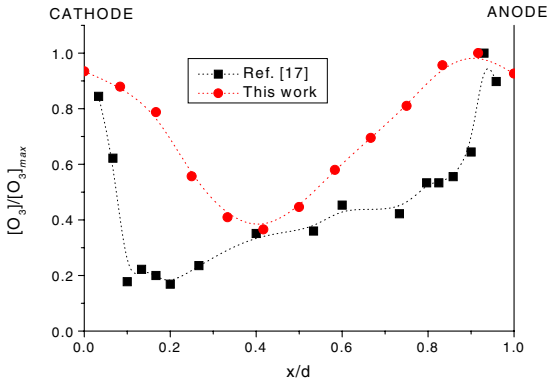

Figure 14. Ozone concentration profiles. Comparison with experimental data [17] (parallel-plane electrode arrangement 'glass–glass', $d = 1.5$ mm, air, $p = 1$ bar, pulsed mode of BD operation).

5. Conclusions

(1) There are three distinct phases of the MD development. The pre-breakdown phase lasts for a period of more than 0.5 μs. It is characterized by a continuous glow on the glass surfaces of both electrodes. During the last 100 ns of the pre-breakdown phase, the maximal light intensity is observed on the anode.
The streamer starts directly from the surface of the anode and crosses the gap with an increasing velocity that reach 10^6 m s^{-1}. Electric field strength of the streamer grows respectively from 120 Td at the anode to 240 Td at the cathode.
The third phase of the MD is a phase of decay of the light and current pulses.

(2) There are two distinct regions with essentially different properties of plasma within the MD channel. The electric field near the cathode is higher than near the anode, and electron density, in contrast, is considerably lower.

(3) It is very important to distinguish between two different modes of BD operation: single pulse and continuous. To provide a correct theoretical description of the MDs for an ordinary continuous mode, a model should be used that takes into account the existence of initially non-uniformly charged dielectric surfaces.

Acknowledgments

This work was supported by the DFG-Sonderforschungsbereich 198, 'Kinetics of Partially Ionized Plasmas'. The authors express their deep gratitude to Frank Miethke (Greifswald, Germany) and Juraj Chlpik (Bratislava, Slovakia) for their contribution to the set-up configuration and to Jan Schäfer (Brno, Czech Republic) for his assistance in performing some spectroscopic measurements.

References

[1] Kogelschatz U, Eliasson B and Egli W 1997 Dielectric barrier discharges—principle and applications *J. Physique IV* C **4** 47–66

[2] Samoilovich V, Gibalov V and Kozlov K 1997 *Physical Chemistry of the Barrier Discharge* (Düsseldorf: DVS)

[3] Kogelschatz U 1999 Industrial ozone production *Proc. Int. Ozone Symp. (Basel, Switzerland)* pp 253–65

[4] Kozlov K V 2000 Physical models of the microdischarge in an ozonizer: classification, analysis, and comparison with the reality *Proc. 7th Int. Symp. on High Pressure Low Temperature Plasma Chemistry (Greifswald, Germany)* vol 2, pp 292–8

[5] Bagirov M A, Nuraliev N A and Kurbanov M A 1972 Discharge in air gap between dielectrics, and number of partial discharges *Sov. Phys.–Tech. Phys.* **17** 495–8

[6] Eliasson B, Hirth M and Kogelschatz U 1987 Ozone synthesis from oxygen in dielectric barrier discharges *J. Phys. D: Appl. Phys.* **20** 1421–37

[7] Braun D, Küchler U and Pietsch G J 1991 Microdischarges in air-fed ozonizers *J. Phys. D: Appl. Phys.* **24** 564–72

[8] Gibalov V I, Samoilovich V G and Filippov Yu V 1981 Physical chemistry of the electrosynthesis of ozone. The results of numerical experiments *Russ. J. Phys. Chem.* **55** 471–9

[9] Eliasson B, Kogelschatz U and Hirth M 1985 The Townsend/streamer transition in a silent discharge in oxygen *Proc. XVII Int. Conf. on Phenomena in Ionized Gases (Budapest, Hungary)* pp 590–2

[10] Yoshida K and Tagashira H 1986 Computer simulation of ozone electrosynthesis in an N_2/O_2 mixture-fed ozonizer *Memoirs Kitami Inst. Technol.* **18** 11–20

[11] Braun D, Hoffman A and Pietsch G 1989 Modelling of microdischarges in ozonizers *Proc. 9th Int. Symp. on Plasma Chemistry (Bari, Italy)* vol 3, pp 751–6

[12] Braun D 1990 Zum Wirkungsgrad von Ozonerzeugern *Thesis* RWTH Aachen, Germany (in German)

[13] Braun D, Gibalov V and Pietsch G 1992 Two-dimensional modelling of the dielectric barrier discharge in air *Plasma Sources Sci. Technol.* **1** 166–74

[14] Gibalov V I and Pietsch G 2000 The development of dielectric barrier discharges in gas gaps and on surfaces *J. Phys. D: Appl. Phys.* **33** 2618–36

[15] Xu X and Kushner M J 1998 Multiple microdischarge dynamics in dielectric barrier discharges *J. Appl. Phys.* **84** 4153–60

[16] Heuser C and Pietsch G 1980 Pre-breakdown phenomena between glass–glass and metal–glass electrodes *Proc. 6th Int. Conf. on Gas Discharges and their Applications (Edinburgh, UK)* pp 98–101

[17] Heuser C 1985 Zur Ozonerzeugung in elektrischen Gasentladungen *Thesis* RWTH Aachen, Germany (in German)

[18] Hirth M, Kogelschatz U and Eliasson B 1983 The structure of the microdischarges in ozonizers and their influence on the reaction kinetics *Proc. 6th Int. Symp. on Plasma Chemistry (Montreal, Canada)* vol 3, pp 663–8

[19] Kozlov K, Shepeliuk O and Samoilovich V 1995 Spatio-temporal evolution of the dielectric barrier discharge channels in air at atmospheric pressure *Proc.11th Int. Conf. on Gas Discharges and their Applications (Tokyo, Japan)* vol 2, pp 142–5

[20] Kozlov K, Shepeliuk O, Monyakin A, Dobryakov V and Samoilovich V 1995 Experimental study of statistical behaviour of separate microdischarges in air-fed ozonizer *Proc. Annual Congress of the Polish Chemistry Society (Lublin, Poland)* pp 79–83

[21] Creyghton Y L M 1994 Pulsed positive corona discharges: fundamental study and application to flue gas treatment *Thesis* TU Eindhoven, The Netherlands

[22] Matveev A A and Silakov V P 1998 Method of calculation of specific radiant emitting of the bands of 1^- and 2^+ systems of nitrogen in the non-equilibrium nitrogen–oxygen plasma *Physics and Technology of Electric Power Transmission* (Moscow: MPEI) pp 201–18 (in Russian)

[23] Djakov A F, Bobrov Yu K, Bobrova L N and Yourguelenas Yu V 1998 Streamer discharge plasma parameters determination in air on a base of a measurement of radiation of the molecular bands of nitrogen *Physics and*

Technology of Electric Power Transmission (Moscow: MPEI) pp 219–33 (in Russian)

[24] Brandenburg R, Kozlov K V Michel P and Wagner H-E 2000 Diagnostics of the single filament barrier discharge in air by cross-correlation spectroscopy *Proc. 7th Int. Symp. on High Pressure Low Temperature Plasma Chemistry (Greifswald, Germany)* vol 1, pp 189–93

[25] Ware W R 1983 Technique of pulse fluorometry *Time-Resolved Fluorescence Spectroscopy in Biochemistry and Biology (NATO ASI Series A: Life Sciences)* vol 69, ed R B Cundall and R E Dale (New York: Plenum) pp 23–57

[26] Shepeliuk O S 1999 Spatio-temporal structure of the microdischarge in an ozonizer and its role in the process of ozone synthesis from air *Thesis* MSU Moscow (in Russian)

[27] Kossyi I A, Kostinsky A Yu, Matveyev A A and Silakov V P 1992 Kinetic scheme of the non-equilibrium discharge in nitrogen–oxygen mixtures *Plasma Sources Sci. Technol.* **1** 207–20

[28] Kozlov K V 1998 Mechanism of barrier discharges in electronegative gases *Proc. 6th Int. Symp. on High Pressure Low Temperature Plasma Chemistry (Cork, Ireland)* pp 288–92

[29] Kozlov K and Pietsch G 1996 Some remarks on the microdischarge development in dielectric barrier discharges *Proc. 5th Int. Symp. on High Pressure Low Temperature Plasma Chemistry (Milovy, Czech Republic)* pp 215–19

[30] Anton H 1966 Zur Lumineszenz einiger Molekülgase bei Anregung durch schnelle Elektronen *Ann. Phys.* **18** 178–93

[31] Millet P, Salamero Y, Brunet H, Galy J and Blanc D 1973 De-excitation of $N_2(C\,^3\Pi_u; \upsilon' = 0$ and 1) levels in mixtures of oxygen and nitrogen *J. Chem. Phys.* **58** 5839–41

[32] Nichols L L and Wilson W E 1968 Optical lifetime measurements using a positive ion van de Graaff accelerator *Appl. Opt.* **7** 167–70

[33] Calo J M and Axtmann R C 1971 Vibrational relaxation and electronic quenching of the $C\,^3\Pi_u(\upsilon' = 1)$ state of nitrogen *J. Chem. Phys.* **54** 1332–41

[34] Mitchell K B 1970 Fluorescence efficiencies and collisional deactivation rates for N_2 and N_2^+ bands excited by soft x-rays *J. Chem. Phys.* **53** 1795–802

[35] Pancheshnyi S V, Starikovskaia S M and Starikovskii A Yu 1997 Measurement of the rate constants of collisional quenching of $N_2(C\,^3\Pi_u)$ and $N_2^+(B\,^2\Sigma_u^+)$ by the molecules N_2, O_2 and CO in afterglow of the nanosecond discharge *Sov. Plasma Phys.* **23** 664–9

[36] Carr T W and Dondes S 1977 Direct measurement of the radiative lifetime and collisional quenching of the $C\,^3\Pi_u$ state of nitrogen as studied by pulsed radiolysis *J. Phys. Chem.* **81** 2225–8

[37] Ikuta N and Kondo K 1976 A spectroscopic study of positive and negative coronas in N_2–O_2 mixture *Proc. 4th Int. Conf. on Gas Discharges and their Applications (Swansea, UK)* pp 227–30

[38] Kondo K and Ikuta N 1980 Highly resolved observation of the primary wave emission in atmospheric positive-streamer corona *J. Phys. D: Appl. Phys.* **13** L33–8

[39] Belikov A E, Kusnetsov O V and Sharafutdinov R G 1995 The rate of collisional quenching of $N_2O(B\,^2\Sigma)$, $N_2^+(B\,^2\Sigma)$, $O_2^+(B\,^4\Sigma)$, $O^+(3d)$, O(3p), $Ar^+(4p')$, Ar(4p, 4p′) at the temperature <200 K *J. Chem. Phys.* **102** 2792–801

[40] Plain A and Jolly J 1984 Quenching rate constants for $N_2^+(B\,^2\Sigma_u^+, \upsilon' = 0, 1, 2)$ with N_2 and Ne *Chem. Phys. Lett.* **111** 133–5

[41] Neff S H 1981 Relative vibrational quenching of $N_2^+(B\,^2\Sigma)$ by N_2 and He *J. Chem. Phys.* **75** 4897–8

[42] Jolly J and Plain A 1983 Determination of the quenching rates of $N_2^+(B\,^2\Sigma_u^+, \upsilon' = 0, 1)$ by N_2 using laser-induced fluorescence *Chem. Phys. Lett.* **100** 425–8

[43] Smith A J, Read F H and Imhof R E 1975 Measurement of the lifetimes of ionic excited states using the inelastic electron-photon delayed coincidence technique *J. Phys. B: At. Mol. Phys.* **18** 2869–79

[44] Dutton J 1975 A survey of electron swarm data *J. Phys. Chem. Ref. Data* **4** 577–85